Using mechanobiological mimicry of red blood cells to extend circulation times of hydrogel microparticles

Timothy J. Merkel[a], Stephen W. Jones[b], Kevin P. Herlihy[a], Farrell R. Kersey[c], Adam R. Shields[d], Mary Napier[a,c,e,f], J. Christopher Luft[a,c,e,f], Huali Wu[g], William C. Zamboni[c,e,g,h], Andrew Z. Wang[c], James E. Bear[b,c,i], and Joseph M. DeSimone[a,c,e,f,g,j,k,l,1]

[a]Department of Chemistry, [b]Cell and Developmental Biology, [c]Lineberger Comprehensive Cancer Center, [d]Physics, [e]Carolina Center of Cancer Nanotechnology Excellence, [f]Institute for Nanomedicine, [g]Eschelman School of Pharmacy, [h]Institute for Pharmacogenomics and Individualized Therapy, [i]Howard Hughes Medical Institute, [j]Institute for Advanced Materials, University of North Carolina, Chapel Hill, NC 27599; [k]Department of Chemical and Biomolecular Engineering, North Carolina State University, Raleigh, NC 27695; and [l]Sloan–Kettering Institute for Cancer Research, Memorial Sloan–Kettering Cancer Center, 1275 York Avenue, New York, NY 10065

It has long been hypothesized that elastic modulus governs the biodistribution and circulation times of particles and cells in blood; however, this notion has never been rigorously tested. We synthesized hydrogel microparticles with tunable elasticity in the physiological range, which resemble red blood cells in size and shape, and tested their behavior in vivo. Decreasing the modulus of these particles altered their biodistribution properties, allowing them to bypass several organs, such as the lung, that entrapped their more rigid counterparts, resulting in increasingly longer circulation times well past those of conventional microparticles. An 8-fold decrease in hydrogel modulus correlated to a greater than 30-fold increase in the elimination phase half-life for these particles. These results demonstrate a critical design parameter for hydrogel microparticles.

biomimetic | deformability | drug carriers | long circulating | red blood cell mimic

The ability of mammalian cells to contract or stretch strongly influences their motility and biodistribution (1). The extraordinary flexibility of mammalian RBCs enables them to deform many thousands of times during their long lives in the circulation with up to 100% strain (2) as they pass through restrictions in the vasculature that is smaller than their diameter. During their 120-d lifetime, RBCs experience chemical changes to their membrane structure, rendering them less flexible, and leading to their removal from the circulation via splenic filtration (3). Beyond RBCs, cancer cells, especially metastatic cancer cells, are elastically softer than healthy cells, a characteristic that is believed to be integral to their ability to spread to new locations (1, 4). Although much attention has been directed toward the enhancement of the circulation time of particles, including alterations of particle size (5, 6), shape (7–9), and surface characteristics (10), the role played by deformability in the in vivo circulation profile of particles has not been well explored.

Though particle size has long been considered dominant in determining in vivo behaviors such as circulation time and biodistribution profile, it stands to reason that physical filtration barriers in the body could be navigated by larger, but more deformable particles (11, 12). Deformable particles that resembled RBCs in size and shape have been shown to deform in restricted channels (13) or capillaries (14) that were smaller than the particle diameter, though the modulus of these particles was not characterized (13) or was poorly matched to RBCs (14) and was restricted to in vitro testing in both cases. In a simulation of renal filtration of soft particles, microgels translocated through pores that were 1/10th of the particle diameter under physiologically relevant pressures (15). Filamentous worm-like micelles were found to have increased circulation times with respect to their spherical counterparts, though this effect was attributed to the size and shape of these particles as well as the deformability (8). Inspired by nature's example of long-circulating microparticles,

we sought to mimic the size and shape of RBCs while varying the modulus across a physiologically relevant range to probe the physical barriers encountered in vivo by soft microparticles. Here we show that increasing the deformability of RBC-sized particles increased their circulation times beyond that of conventional microparticles and significantly altered their biodistributions. We found that, as a consequence of their low modulus, these discoid microparticles bypassed several in vivo filtration mechanisms, illustrated by animal survival and dramatic increases in elimination half-lives of particles with decreasing modulus. Such deformable and long-circulating particles may find utility in the fields of drug delivery and medical imaging, where long-circulation times and varied biodistributions are often desirable characteristics (6, 16, 17). Further, we expect these results will stand as an introduction for particle deformability as a vital design parameter that can affect the behavior of particles on both the micro- and nanoscales.

Results and Discussion

Fabrication of Red Blood Cell Mimics (RBCMs). The particle replication in nonwetting templates (PRINT®) technique that has been developed in our laboratory allows for the fabrication of nonspherical, shape-specific particles through use of elastomeric fluoropolymer molds (18, 19). Using PRINT, we fabricated particles with similar size, shape, and deformability characteristics as RBCs (Fig. 1). In this study we chose to model the 6-μm diameter mouse RBC (20) and observe the in vivo behavior of the RBCMs. Although the distinctive biconcave discoidal shape of mature RBCs is generally conserved throughout the animal kingdom, mouse RBCs (6-μm diameter) are slightly smaller than their human counterparts (8-μm diameter) (20). Many hydrogels exhibit excellent biocompatibility (21), with their swelling and deformability controllable by varying the amount of cross-linking in the gel (22). We used hydrogels composed primarily of 2-hydroxyethyl acrylate (HEA) that were lightly (1–10%, by weight) cross-linked with poly(ethylene glycol) diacrylate (PEGDA, MW = 4,000 g/mol) with a photoinitiator (1-hydroxycyclohexyl

Fig. 1. RBCM particles. (*A*) A graphical depiction of the PRINT process used to fabricate RBCMs. Briefly (*Top* to *Bottom*), an elastomeric fluoropolymer mold (green) with disc-shaped wells was covered by an aliquot of the prepolymer mixture (red). The mold was passed through a pressured nip (black) covered by a high-energy sheet (gray), wicking away excess liquid from the mold surface while filling the wells of the mold. The filled mold was cured photochemically, yielding cross-linked hydrogel particles, which were harvested from the mold by freezing onto a thin film of 1% poly(vinyl alcohol) in water (blue) and peeling away the mold. Melting of this layer resulted in a suspension of hydrogel particles. (*B*–*E*) Fluorescent images of hydrated RBCMs with varying percent cross-linker; (*B*) 10% cross-linked, (*C*) 5% cross-linked, (*D*) 2% cross-linked, and (*E*) 1% cross-linked. Scale bars are 20 μm.

phenyl ketone), and polymerizable fluorescent dyes (1%) to facilitate imaging. To mimic the negatively charged RBC membrane, we added 2-carboxyethyl acrylate (10%). See Table S1 for further details on hydrogel composition.

To evaluate the suitability of this hydrogel for RBCM particles, we hydrated macroscopic coupons of hydrogels with varying percentage of PEGDA cross-linker at neutral pH and tested their mechanical properties with an Instron 5556 Universal Testing Machine (Instron) with a strain rate of 5 mm/min. For bulk modulus studies we used fluorescein-o-acrylate as the polymerized dye, and to improve depth of tissue penetration and avoid tissue autofluorescence, a near-IR dye (Dylight$_{680}$maleimide) was used for in vivo applications. By lowering the amount of cross-linker from 10% to 1%, we tuned the modulus of the resultant hydrated polymer from 63.9 to 7.8 kPa, respectively (Table 1), overlapping the range of the reported modulus for RBCs (26 ± 7 kPa) (23).

Because of the swelling observed in the bulk hydrogel samples, we designed scaled-down master templates and molds for this study. The scaled-down features of the molds, with diameters of 2 or 3 μm, allowed the RBCMs to swell to the desired dimensions upon hydration, yielding discs that were 5.2–5.9 μm in diameter and 1.22–1.54 μm tall, with the feature size and final RBCM dimensions dependent upon the percent of cross-linker and the mold used. Filling the molds resulted in a meniscus, leaving the particles thinner in the middle and thicker at the edges (Fig. 1). This effect, which is not uncommon for the PRINT method (9), yielded RBCMs that were reminiscent of the biconcave shape of RBCs.

To assess the biocompatibility of the RBCMs, we performed in vitro cytotoxicity assays on human umbilical vein endothelial cell (HUVEC) (endothelial) cells. We dosed cells with varied concentrations of RBCMs (1.5–200 μg/mL) and incubated for 72 h (Fig. S1) before performing both MTS [(3-(4,5-dimethylthiazol-2-yl)-5-(3-carboxymethoxyphenyl)-2-(4-sulfophenyl)-2H-tetrazolium)] and ATP-luciferase assays to assess cell life. Particles were well tolerated at all dosages tested by both assays. To examine the interaction of RBCMs with endothelial cells, we performed a flow cytometry-based cell uptake experiment (24). RBCMs were dosed to HUVEC cells at a concentration of 15 μg/mL and in-

cubated for 15 min, 1, 2, 4, and 24 h, and then evaluated to determine the percentage of cells that had internalized the RBCM particles. Interaction between the RBCMs and cells was minimal, with less than 10% of cells having internalized particles after 24 h of incubation time (Fig. S2).

Microfluidic Examination of Particle Deformability. To demonstrate the ability of RBCMs to deform in flow conditions such as they might experience in traversing the microvasculature, we utilized a microfluidic device with constricted pores (Fig. 2). Microfluidic models of vascular constriction have been explored to evaluate the behavior of natural and diseased RBCs (25) and synthetic mimics of RBCs (13). We designed a 3-μm tall channel with pores that were 3 μm wide and 50 μm long and repeated many times over the length of the device. The height of the channels was too short for the RBCMs to orient vertically to pass through the restrictions, forcing the particles to deform in order to traverse the pores. The device design (Fig. 2*A*) included over 100 repetitions of 3-μm restricted pores over the length of the channel, as well as an unrestricted 15-μm path on each side of the restrictions, running the length of the channel. This architecture tested the ability of the particles to deform repeatedly while providing an unobstructed path for fluid flow to maintain reasonably low pressures through the constricted pathways. Although the smallest capillaries in the body have diameters of around 5 μm, RBCs routinely deform to traverse splenic sinusoids that are much smaller (26). When dilute solutions of RBCMs were flowed through the device at a constant flow rate (0.06 mL/min), the lower modulus RBCMs (1 and 2% cross-linked) navigated these pores, whereas more rigid RBCMs rapidly clogged them (Fig. 2). A movie of 1% cross-linked RBCMs traversing these pores can be seen in *SI Text* (Movie S1). In flow, the 1% cross-linked RBCMs stretched in the 3-μm wide channels, increasing in length $239\% \pm 26\%$ ($n = 15$) while flowing through the restricted channels, followed by a relaxation back to their original discoid shape in the absence of flow. This behavior is similar to that of natural RBCs, which deform under flow conditions and only fully resume their characteristic discoid shape once flow is halted (27). Although RBCMs have similar size, shape, and deformability to RBCs, they differ

Table 1. Modulus values and compartmental analysis of RBCM particles from intravital microscopy experiments

% Cross-linker	Modulus of bulk material, kPa	Distribution half-life, h	Elimination half-life, h	AUC, fluoresence* h	Average R^2
10%	63.9 ± 15.7	0.038 ± 0.0012	2.88 ± 0.92	0.65 ± 0.14	0.8966
5%	39.6 ± 10.4	0.066 ± 0.036	5.12 ± 2.17	0.76 ± 0.57	0.9029
2%	16.9 ± 1.7	0.15 ± 0.025	7.12 ± 0.82	1.35 ± 0.26	0.9468
1%	7.8 ± 1.0	0.35 ± 0.13	93.29 ± 31.09	15.44 ± 15.63	0.9330

*Ranges given represent one standard deviation. Values were derived from scans of three mice.

Fig. 2. Microfluidic evaluation of RBCM deformability. (*A*) A schematic of the microfluidic devices, with flow driven by a syringe pump. (*B*) An image sequence showing a 1% cross-linked RBCM (6.0-μm diameter) deforming to pass through a 3 × 3.5 μm channel (25 ms between frames). (*C*) Ten percent cross-linked RBCMs stuck in the entrance of the 3-μm pores in a microfluidic device. Scale bars are 30 μm.

in fundamental structure: RBCs are fluid-filled sacs contained by a complex membrane that has extreme flexibility originating from the membrane structure (28, 29), whereas the RBCMs are uninterrupted hydrogel discs. These two disparate structures should have different behaviors and mechanisms of deformation in constricted flow (13) though further studies are needed to elucidate these details for the RBCMs.

Compartmental Analysis of RBCM Circulation Profile After Intravenous Administration. We used an intravital imaging method to examine the behavior of RBCMs when intravenously injected into mice. For intravital approaches, the microcirculation is directly observed with high spatial and temporal resolution, often through the use of surgical techniques to expose tissues of interest (30, 31). In our approach, we observed the peripheral vasculature through the skin of an anesthetized mouse's ear. We directly observed the RBCMs via the near-IR fluorescence of the particles by imaging every 2 s for 2 h as the particles traversed this portion of the vasculature (see Movies S2 and S3). Elimination curves were generated by tracking the change in fluorescent signal from the particles over time (Fig. 3), normalizing each scan to the max-

imum intensity slice and plotting decay as a function of this maximum intensity.

Several pharmacokinetic models were investigated using a standard pharmacokinetic modeling program [WinNonlin (version 5.2.1; Pharsight Corp.)] to describe the plasma concentration versus time profiles to determine the best model. One- and two-compartment models with elimination from the central compartment, from the software's library, were investigated, as was a two-compartment model with elimination from both the central and peripheral compartments, which was built by our group. The evaluation of the goodness of fit was based on the Akaike information criterion, the variability of the parameter estimates, and the absence of a significant correlation between independent model parameters (<0.95). The two-compartment model with one elimination step from the central compartment provided the best fit for all of the datasets examined.

To evaluate the kinetics of RBCM clearance, we used this two-compartment pharmacokinetic model, characterized by a biexponential decrease in particle concentration over time (32), with parameters fit by nonlinear regression analysis (33). This model describes an initial (distribution) phase where the particles

Fig. 3. Intravital microscopy data and compartmental analysis. (*A*) Vasculature highlighted with rhodamine B labeled dextran prior to injection of RBCMs. (*B*) Dylight 680 labeled 1% cross-linked RBCMs flowing through this stretch of vasculature 20 min after dosing, with ROI outlined in yellow. (*C*) Colored overlay of *A* and *B*, with dextran in blue and particles shown in red. Scale bars are 100 μm. (*D*) Two-compartment model schematic and governing equations used to fit the data. (*E*) Decrease in fluorescent signal in the ROI for the 2-h scan in this mouse. The semilog plot shows calculated fit for the two-compartment pharmacokinetic models.

$$Cp = Ae^{-\alpha t} + Be^{-\beta t}$$

$$A = \frac{D(\alpha - k_2)}{V_C(\alpha - \beta)}$$

$$B = \frac{D(k_2 - \beta)}{V_C(\alpha - \beta)}$$

Where C_P is the plasma concentration, α is the hybrid first order rate constant for the distribution process, β is the hybrid first order rate constant for the elimination process, D is the dose administered, and V_C is the volume of the central compartment.

Merkel et al.

distribute from the plasma into various tissues, followed by a late (elimination) phase that describes the ultimate clearance of particles from the plasma (Fig. 3). For small molecules and nanoparticles the distribution is attributed to extravasation into tissue; because of their size, the distribution of RBCMs may be due to physical entrapment in constricted capillaries or tissues with low blood flow rather than by an extravasation process. Although we observed the RBCMs only for the initial 2 h in vivo, the uncertainty associated with the mathematical fitting was minimized due to the large number of data points used to fit each curve (over 350). Calculated distribution and elimination half-lives ($t_{1/2(\alpha)}$ and $t_{1/2(\beta)}$, respectively) trended to longer times with decreased modulus (Table 1). Although the least flexible RBCMs were cleared quite rapidly, circulation times increased with increasing particle elasticity, with the most deformable RBCMs eliminated over 30 times more slowly than their most rigid counterparts ($t_{1/2(\beta)} = 3.9$ d).

Intravital microscopy provided a method for direct observation of RBCM particles in the peripheral vasculature of mice and allowed us to make a close and thorough examination of the initial clearance profiles of these particles. Our analysis provided curves with approximately 350 data points illustrating the elimination of these particles from the circulation over each 2-h scan. Nonlinear regression analysis yielded excellent fits, with the large number of data points adding a measure of certainty to the shape defined by these elimination curves. With a method of directly observing the particles, we expect that our detection limits should be quite low as we are able to discern individual particles in the scans. However, this method was not without limitations. Direct correlation of the intensity of the fluorescent signal of the particles to a particle concentration was difficult due to several factors, including variabilities in the depth, volume, and flow rates in observed portions of vasculature and the relatively fast movement of particles relative to the scanning speed of the microscope. Lacking the correlation to particle concentration, we were unable to perform a full pharmacokinetic analysis on the RBCMs examined, though much was learned through an analysis of the shape of these curves.

To verify the long-circulating behavior of 1% cross-linked RBCMs, we tracked particle concentration in blood at time points out to 5 d postinjection via a more traditional blood-draw method. We examined three mice per time point, including 2, 8, 24, 72, and 120 h postinjection. At each time point examined, we sacrificed the mice, collected blood via cardiac puncture, and measured the fluorescent signal from the particles in the whole blood, which was correlated to concentration through the generation of a standard curve (see *SI Text*). Pharmacokinetic analysis of these data by the two-compartment model discussed above was in good agreement with the data obtained from the intravital technique; both techniques showed a fairly rapid distribution of the majority of the dose to various tissues, with 10–15% remaining in the blood after 2 h, resulting in an elimination half-life of 3.6 d, with 5% of the injected dose remaining in the blood after 5 d (Table 2).

Biodistribution of RBCM Particles After Intravenous Injection. To examine the biodistribution of RBCMs with changing deformability, we sacrificed the mice 2 h postinjection and harvested tissue and blood samples for further analysis. Tissue samples were not perfused prior to analysis. Five and 10% cross-linked RBCMs distributed primarily into the capillary beds in the lungs (Fig. 4). This behavior is typical for intravenously injected micro-particles,

with the bulk of the dose most likely sequestered immediately postinjection as this is the first downstream tissue with microvasculature. These stiffer RBCMs were poorly tolerated, with significant distress requiring sacrifice of some mice prior to scan completion; presumably due to the stiff particles contributing to pulmonary embolism. More flexible RBCMs (1 and 2% cross-linker) were very well tolerated, presumably due to the avoidance of filtration in the lungs. Mice that were sacrificed early were not included in any datasets presented here, as the time postinjection was incongruent with the bulk of the data analyzed. The most deformable RBCMs (1% cross-linked) were primarily sequestered in the spleen (67% recovered fluorescence/g), having largely avoided filtration in the lungs. Lung filtration was largely avoided by particles with 2% or less cross-linker ($\leq$16.9 kPa, bulk material), suggesting that the modulus of these materials may indicate a threshold value for avoidance of filtration by the lungs. Uptake in the kidneys was significant for all but the 1% cross-linked RBCMs, though further studies will be required to elucidate the mechanism of this clearance.

Distribution of 1% cross-linked RBCMs in liver, lung, spleen, kidneys, and blood was tracked for 2, 8, 24, 72, and 120 h postinjection (Figs. S4 and S5). Saturation of tissues occurred at different times, indicating a redistribution of particles after some initial distribution at the time of dosing. Although splenic accumulation peaked at 24 h, signal in the lungs decreased over the time course of the experiment; suggesting a delayed release of the physically entrapped particles back into the circulation.

With approximately 5% of the cardiac output flowing through the spleen (3) and the total blood volume of the mouse circulating 7–8 times per minute (34), the whole blood volume was passed through the mouse spleen some 42–48 times over the course of our 2-h scans. The continued persistence of 1% cross-linked RBCMs in the circulation after this time suggests that splenic accumulation may be due in part to long residence time rather than permanent filtration, as is the case for RBCs, where filtration occurs first as an effect of slow blood flow through the macrophage containing red pulp, followed by physical filtration when passing through the sinusoids or transmural apertures (3).

Further studies will be required to illuminate the capability of these particles to carry and deliver therapeutic payloads; however, extremely low modulus RBCMs could have therapeutic applications for splenic disorders due to their preferential accumulation in this tissue and the have potential for drug delivery applications due to their long-circulation times and low accumulation in the liver. Drug dosing can be limited by toxicity to a clearance organ such as the liver (35, 36). The apparent splenic clearance of RBCMs affords the possibility of different dosing restrictions if these particles were to be used as drug carriers because of the low concentrations found in the liver, as well as the possibility for direct treatment or imaging of the spleen. The most deformable of the RBCMs tested here successfully navigated regions of constricted blood flow, resulting in extended circulation times and illuminating a critical design parameter for microparticles. Further experimentation with extremely deformable materials on different size scales—from tens of nanometers to the 6-μm diameter particles used in this study, should cast light on the role played by deformability in enhancing the circulation times of biologically relevant particles.

Materials and Methods

Materials. Commercially available HEA (96%, Aldrich) contains impurities such as acrylic acid, ethylene glycol, and ethyleneglycol diacrylate (EGDA)

Table 2. Pharmacokinetic parameters for 1% cross-linked RBCMs calculated from blood draws taken out to 5 d postinjection

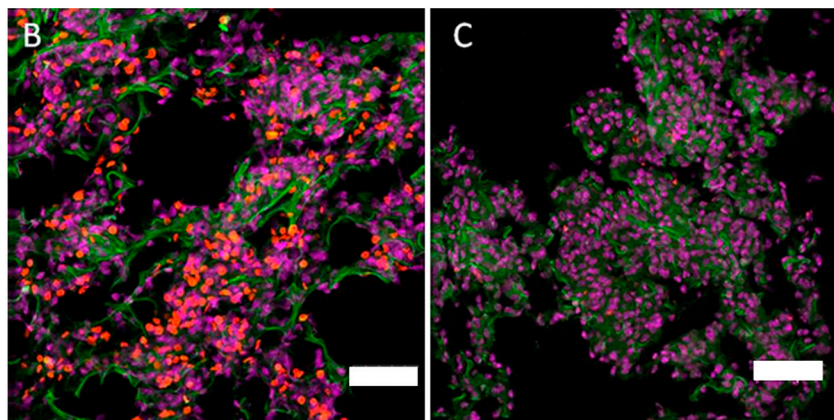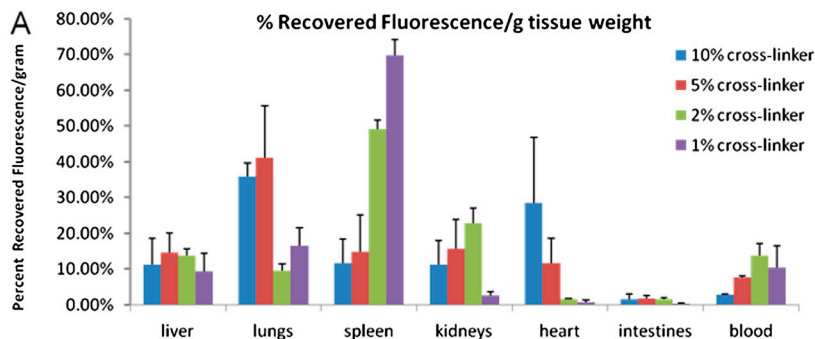| A, mg/mL	B, mg/mL	α, h^{-1}	β, h^{-1}	$\alpha t_{1/2}$, h	$\beta t_{1/2}$, h	V_C, mL	AUC, mg*h/mL	CL$_T$, mL/h	Vd$_\beta$, mL
0.190	0.0482	0.241	0.00768	2.876	90.235	2.934	7.067	0.0990	12.894

Fig. 4. Biodistribution of RBCMs. (*A*) Distribution of RBCMs into various tissues 2 h postdosing by percent recovered fluorescence normalized for tissue weight. Error bars represent one standard deviation, with $n = 3$ for each case. (*B*) Lung tissue from a mouse dosed with 10% cross-linked RBCMs. Particles are shown in red, with cell nuclei in purple, and cytoskeleton (F-actin) stained green. (*C*) Lung tissue from a mouse dosed with 1% cross-linked RBCMs, with tissue stained as in *B*. Very few RBCMs were in this tissue compared to mice dosed with more rigid particles, consistent with the tissue distribution data. Scale bars are 50 μm.

and was purified prior to use according to the procedure set forth by Elif and Ali (37). Briefly, HEA was dissolved in water (25% by volume) and the solution extracted 10 times with hexanes. Salt (200 g of NaCl/L) was added to the aqueous phase, and the monomer was extracted by washing with ether (4 times). The solution was dried with MgSO$_4$ (3 wt %), and ether was removed by rotary evaporator. The purified monomer was distilled under vacuum prior to use. PEG 4000 diacrylate (DA) (Polysciences, Inc.), 2-carboxyethyl acrylate (Aldrich), fluorescein-o-acrylate (97%, Aldrich), 1-hydroxycyclohexyl phenyl ketone (99%, Aldrich), Dylight 680 maleimide (Thermo Scientific), Fluorescein-o-acrylate (97%, Aldrich) and methacryloxyethyl thiocarbamoyl rhodamine B (PolyFluor 570, Polysciences, Inc.) were used as received. All other materials were used as received, unless otherwise noted.

Modulus Testing. To measure the mechanical properties of the cross-linked HEA hydrogels, we polymerized macroscopic coupons of the prepolymer mixtures described in Table S1 via UV light ($\lambda = 365$ nm, power = 20 mW/cm^2) in a Teflon mold. The cross-linked hydrogels were removed from the mold, weighed, and then placed in pH 7.4 PBS buffer for 24 h to fully hydrate. The coupons were patted dry with paper towels and weighed again prior to testing with an Instron 5556 Universal Testing Machine (Instron) with a strain rate of 5 mm/min.

Particle Fabrication. For the PRINT technique (9, 18), master templates were prepared via traditional photolithography to have ordered arrays of raised discs with low aspect ratios, mimicking the shape of RBCs. A photocurable perfluoropolyether (Fluorocur, Liquidia Technologies) was drop cast onto a master template, and a flexible plastic sheet was applied to the top of the resin to act as a supportive backing for the mold that resulted from photocuring of the resin and subsequent removal from the master template. The master templates and molds used in this study had discoid features with 2- and 3-μm diameters and heights of 0.6 and 0.9 μm, respectively, and produced particles with 5- to 6-μm diameters due to swelling of the particle hydrogel material. For the fabrication of the particles, the prepolymer mixture was spread onto a mold that was chilled to 2–5 °C on a custom-built laminator platform. The reduced temperature prevented evaporation of the prepolymer solution prior to photocuring. A poly(ethylene terepthalate) (PET) sheet was laminated to the top of the mold and prepolymer solution, wetting the total mold area. The sheet was peeled away at the nip point of the laminator, leaving the wells of the mold filled while wicking away excess solution. The filled mold was immediately transferred into a chilled (2–5 °C), nitrogen purged UV oven and cured with UV light ($\lambda = 365$ nm,

power = 20 mW/cm^2). After curing, the filled mold was placed face down on a thin film of 0.1% 2,000 g/mol poly(vinyl alcohol) (PVOH, Acros) in water on top of another PET sheet. This assembly was placed in a −80 °C cooler, allowing the water to freeze and adhere to the particles. After freezing, the mold was peeled away from the particles trapped in the ice layer, and the ice was allowed to melt. RBCMs and water were collected, then washed and concentrated via tangential flow filtration with a MicroKros hollow fiber filter (500 kDa, Spectrum Laboratories, Inc.) to remove any sol fraction from solution. Particles were then suspended in 0.1% 2,000 g/mol PVOH in PBS, pH 7.4 for subsequent experiments.

Particle Characterization. These methods (confocal microscopy, cell viability, cell uptake, and zeta potential) are described in *SI Text*, Figs. S1 and S2, and Table S2.

Microfluidics. Microfluidic devices were fabricated from silicone (Sylgard 184, Dow Corning) sealed to glass after treatment with oxygen plasma, with flow driven by a syringe pump at a fixed rate (0.06 μL/min). Dilute solutions of 1% cross-linked RBCMs (1–5 μg/mL in PBS with 0.1% PVOH) were pumped through the channel and observed with a fluorescence microscope (Nikon TE2000). Videos were taken with a with a Photometrics Cascade II:512 camera. Particle stretching was analyzed with ImageJ software.

Intravital Microscopy. Intravital microscopy experiments were performed using an IV 100 laser scanning microscope (Olympus) on female BALB/c mice of 22- to 26-g body weight (Harlan Sprague Dawley). Hair was removed from the ear and a tail vein catheter was applied. The mice were anesthetized with isofluorane and placed onto a heated stage (37 °C) in a prone position, with an ear immobilized by taping to an aluminum block. Vasculature was located by injection with a solution of 20 mg/mL rhodamine B labeled 70-kDa dextran (Invitrogen) in PBS and visualized by excitation with a 568-nm laser. A suspension of RBCMs, 33 mg particles/kg mouse weight via a 3.5 mg/mL solution of RBCMs in PBS with 0.1% PVOH, was then injected and visualized using a 633-nm laser. Controls were injected with the dextran solution followed by 200 μL of PBS with 0.1% poly(vinyl alcohol). Imaging scans proceeded for 2 h, with an image taken every 2 s. For analysis of the circulation persistence of the particles, the image files from each scan were exported to imageJ. For ease of analysis, we followed the example of Tong et al. (38) and stacked the images in groups of 10. We analyzed the region of interest containing vasculature for fluorescent signal in each scan and corrected for variation in laser intensity or autofluorescence by background correcting each image with the signal from a region of the scan that was free of vas-

culare. For comparison, we normalized each scan to the maximum intensity slice for that scan, providing curves that measured the clearance of particles from the peripheral vasculature over time as a percentage of the maximum signal. Further details are outlined in *SI Text*.

Controls and dosed mice were sacrificed 2 h after injections, and blood and tissues were harvested for imaging. Harvested tissues including liver, lung, spleen, kidneys, heart, and intestines were weighed, then imaged using an IVIS Kinetic fluorescence imaging system (Caliper Life Sciences) with excitation at 675 nm and emission measured at 720 nm. Blood was harvested via cardiac puncture and pipetted in 100-μL aliquots to black 96-well plates for analysis on the imager. The fluorescent signal for each tissue sample was background corrected by subtracting the signal from control tissues. Biodistribution profiles for the RBCMs at 2 h postdose were determined by percent of recovered fluorescence in the above tissues (Fig. 4). Fluorescent signal in the blood was calculated by measuring the fluorescent signal from several aliquots of blood and extrapolating to account for the total blood volume in the mice (approximately 1.7 mL/20 g of body weight) (39).

Biodistribution. Harvested blood was analyzed for fluorescent signal with an IVIS Kinetic imager with excitation at 675 nm and emission measured at 720 nm, and concentrations were calculated with a standard curve. Harvested

tissues were analyzed as above, with biodistribution profiles presented as a percent of the recovered fluorescence per gram of tissue weight.

Blood-Draw Experiments. For evaluation of longer time points, particles were injected as in the previously described study, with mice sacrificed at the indicated time points by cardiac puncture. Fluorescent signal from harvested blood was measured as above, with concentrations determined from a standard curve resulting from serial dilutions of particles in mouse blood (Fig. S2).

Hisology. Details of the procedure for staining and imaging the harvested tissues are found in *SI Text*.

Pharmacokinetic Analysis. Further details on the pharmacokinetic analysis carried out for the RBCMs can be found in *SI Text*.

1. Suresh S (2007) Biomechanics and biophysics of cancer cells. *Acta Biomater* 3:413–438.
2. Fung YC (1993) *Biomechanics Mechanical Properties of Living Tissues* (Springer, New York), 2nd Ed, p 121.
3. Bowdler AJ, ed. (2002) *The Complete Spleen. Structure, Function, and Clinical Disorders* (Humana Press, Totowa, NJ), 2nd Ed, 140,, pp 18–20–30–47.
4. Suresh S (2007) Nanomedicine: Elastic clues in cancer detection. *Nature Nanotechnol* 2:748–749.
5. Champion JA, Walker A, Mitragotri S (2008) Role of particle size in phagocytosis of polymeric microspheres. *Pharm Res* 25:1815–1821.
6. Kohane DS (2007) Microparticles and nanoparticles for drug delivery. *Biotechnol Bioeng* 96:203–209.
7. Champion JA, Katare YK, Mitragotri S (2007) Particle shape: A new design parameter for micro- and nanoscale drug delivery carriers. *J Control Release* 121:3–9.
8. Geng Y, et al. (2007) Shape effects of filaments versus spherical particles in flow and drug delivery. *Nature Nanotechnol* 2:249–255.
9. Gratton SE, et al. (2008) The effect of particle design on cellular internalization pathways. *Proc Natl Acad Sci USA* 105:11613–11618.
10. Drummond DC, Meyer O, Hong K, Kirpotin DB, Papahadjopoulos D (1999) Optimizing liposomes for delivery of chemotherapeutic agents to solid tumors. *Pharmacol Rev* 51:691–743.
11. Fox ME, Szoka FC, Frechet JM (2009) Soluble polymer carriers for the treatment of cancer: The importance of molecular architecture. *Acc Chem Res* 42:1141–1151.
12. Mitragotri S, Lahann J (2009) Physical approaches to biomaterial design. *Nat Mater* 8:15–23.
13. Haghgooie R, Toner M, Doyle PS (2009) Squishy non-spherical hydrogel microparticles. *Macromol Rapid Comm* 31:128–134.
14. Doshi N, Zahr AS, Bhaskar S, Lahann J, Mitragotri S (2009) Red blood cell-mimicking synthetic biomaterial particles. *Proc Natl Acad Sci USA* 106:21495–21499.
15. Hendrickson GR, Lyon LA (2010) Microgel translocation through pores under confinement. *Angew Chem Int Edit* 49:2193–2197.
16. Alexis F, Pridgen E, Molnar LK, Farokhzad OC (2008) Factors affecting the clearance and biodistribution of polymeric nanoparticles. *Mol Pharmacol* 5:505–515.
17. Canelas DA, Herlihy KP, DeSimone JM (2009) Top-down particle fabrication: Control of size and shape for diagnostic imaging and drug delivery. *Wiley Interdiscip Rev Nanomed Nanobiotechnol* 1(4):391–404.
18. Merkel TJ, et al. (2009) Scalable, shape-specific, top-down fabrication methods for the synthesis of engineered colloidal particles. *Langmuir* 26:13086–13096.
19. Rolland JP, et al. (2005) Direct fabrication and harvesting of monodisperse, shape-specific nanobiomaterials. *J Am Chem Soc* 127:10096–10100.
20. Snyder GK, Weathers WW (1977) Hematology, viscosity, and respiratory functions of whole blood of the lesser mouse deer, Tragulus javanicus. *J Appl Physiol* 42:673–678.
21. Nguyen KT, West JL (2002) Photopolymerizable hydrogels for tissue engineering applications. *Biomaterials* 23:4307–4314.
22. Rehfeldt F, Engler AJ, Eckhardt A, Ahmed F, Discher DE (2007) Cell responses to the mechanochemical microenvironment—implications for regenerative medicine and drug delivery. *Adv Drug Deliver Rev* 59(13):1329–1339.
23. Dulinska I, et al. (2006) Stiffness of normal and pathological erythrocytes studied by means of atomic force microscopy. *J Biochem Biophys Methods* 66:1–11.
24. Fattorossi A, Nisini R, Pizzolo JG, D'Amelio R (1989) New, simple flow cytometry technique to discriminate between internalized and membrane-bound particles in phagocytosis. *Cytometry* 10:320–325.
25. Shevkoplyas SS, Yoshida T, Gifford SC, Bitensky MW (2006) Direct measurement of the impact of impaired erythrocyte deformability on microvascular network perfusion in a microfluidic device. *Lab Chip* 6:914–920.
26. Cho Y, De Bruyn PP (1975) Passage of red blood cells through the sinusoidal wall of the spleen. *Am J Anat* 142:91–105.
27. McWhirter JL, Noguchi H, Gompper G (2009) Flow-induced clustering and alignment of vesicles and red blood cells in microcapillaries. *Proc Natl Acad Sci USA* 106:6039–6043.
28. Li J, Lykotrafitis G, Dao M, Suresh S (2007) Cytoskeletal dynamics of human erythrocyte. *Proc Natl Acad Sci USA* 104:4937–4942.
29. Park Y, et al. Measurement of red blood cell mechanics during morphological changes. *Proc Natl Acad Sci USA* 107:6731–6736.
30. Sandanaraj BS, Gremlich HU, Kneuer R, Dawson J, Wacha S (2010) Fluorescent nanoprobes as a biomarker for increased vascular permeability: Implications in diagnosis and treatment of cancer and inflammation. *Bioconjugate Chem* 21:93–101.
31. Smith BR, et al. (2008) Real-time intravital imaging of RGD-quantum dot binding to luminal endothelium in mouse tumor neovasculature. *Nano Lett* 8:2599–2606.
32. Neubauer AM, et al. (2008) Nanoparticle pharmacokinetic profiling in vivo using magnetic resonance imaging. *Magn Reson Med* 60:1353–1361.
33. Brown AM (2001) A step-by-step guide to non-linear regression analysis of experimental data using a Microsoft Excel spreadsheet. *Comput Method Programs Biomed* 65:191–200.
34. Janssen B, Debets J, Leenders P, Smits J (2002) Chronic measurement of cardiac output in conscious mice. *Am J Physiol Regul Integr Comp Physiol* 282:R928–935.
35. Bissell DM, Gores GJ, Laskin DL, Hoofnagle JH (2001) Drug-induced liver injury: Mechanisms and test systems. *Hepatology* 33:1009–1013.
36. Lee WM, Senior JR (2005) Recognizing drug-induced liver injury: Current problems, possible solutions. *Toxicol Pathol* 33(1):155–164.
37. Elif V, Ali U (2005) Polymerization of 2-hydroxyethyl acrylate in bulk and solution by chemical initiator and by ATRP method. *J Polym Sci Pol Chem* 43:3957–3965.
38. Tong L, He W, Zhang Y, Zheng W, Cheng JX (2009) Visualizing systemic clearance and cellular level biodistribution of gold nanorods by intrinsic two-photon luminescence. *Langmuir* 25:12454–12459.
39. Gratton SE, et al. (2007) Nanofabricated particles for engineered drug therapies: A preliminary biodistribution study of PRINT nanoparticles. *J Control Release* 121:10–18.

BIOPHYSICS AND COMPUTATIONAL BIOLOGY